RESEARCH ARTICLE | APRIL 10 2026

Electrode optimization for efficient resonant electro-optic frequency microcombs

S. Häusler ; A. Volpini ; G. Finco ; G. Li ; C. Caër ; J. S. Holzer ; H. Sattari ; H. Zarebidaki ; I. Prieto ; S. Lecomte ; R. Grange ; C. Wildfeuer ; D. Grassani

APL Photonics 11, 046109 (2026)
https://doi.org/10.1063/5.0312190

Electrode optimization for efficient resonant electro-optic frequency microcombs

Cite as: APL Photon. 11, 046109 (2026); doi: 10.1063/5.0312190
Submitted: 14 November 2025 • Accepted: 9 March 2026 •
Published Online: 10 April 2026

S. Häusler,[1,a] A. Volpini,[2,a] G. Finco,[3] G. Li,[3] C. Caër,[2] J. S. Holzer,[2] H. Sattari,[2] H. Zarebidaki,[2] I. Prieto,[2] S. Lecomte,[2] R. Grange,[3] C. Wildfeuer,[1] and D. Grassani[2]

AFFILIATIONS

[1] University of Applied Sciences and Arts Northwestern Switzerland (FHNW), Institute for Sensors and Electronics, Klosterzelgstrasse 2, CH-5210 Windisch, Switzerland

[2] Swiss Center for Electronics and Microtechnology (CSEM), Rue de l'Observatoire 58, CH-2000 Neuchâtel, Switzerland

[3] ETH Zurich, Department of Physics, Institute for Quantum Electronics, Optical Nanomaterial Group, Auguste-Piccard-Hof 1, CH-8093 Zurich, Switzerland

[a] **Authors to whom correspondence should be addressed:** samuel.haeusler@fhnw.ch and andrea.volpini@csem.ch

ABSTRACT

Resonant electro-optic comb generation in thin-film lithium niobate microrings is a powerful method for achieving large-bandwidth electro-optic combs with a small footprint. While significant progress has been made in optimizing the optical resonator, the on-chip microwave waveguide has been less explored. Here, we develop a generic analytical model that predicts the phase shift acquired by the optical wave, taking into account possible microwave losses, impedance and velocity mismatches, and different injection points. We apply this model to determine the optimal electrode length for a traveling-wave configuration and two standing-wave configurations, with microwave driving frequencies at different multiples of the optical free spectral range. We experimentally validate the model by measuring several devices fabricated at the chip and wafer levels.

I. INTRODUCTION

Nonlinear crystals exhibiting a large Pockels coefficient, such as lithium niobate, have enabled the development of high-speed electro-optic (EO) modulators in fiber optics.[1] In optical resonators, these modulators have led to the generation of stable optical frequency combs.[2] The availability of thin-film lithium niobate (TFLN) on insulator wafers,[3,4] combined with the ability to pattern low-loss waveguides,[5] has dramatically reduced the footprint of such devices and unlocked better performance via dispersion engineering[6] and tighter confinement of the optical modes. In addition, several foundries are now offering TFLN-based photonic integrated circuits (PICs), allowing integration of such devices in larger circuits with potential applications in fields such as gas sensing,[7] metrology,[8] optical communication,[9] and more.[10,11]

Resonant EO combs are generated by phase modulating a continuous-wave optical pump in a cavity with resonances that are equally spaced in frequency. When the pump is at resonance, the phase modulation produces sidebands around the pump frequency f_o shifted by the modulation frequency f_m (angular frequency $\omega_m = 2\pi f_m$). If f_m coincides with a multiple of the free spectral range (FSR) of the cavity ($f_m = k \cdot \mathrm{FSR}$), the sidebands are also in resonance. As a result, new lines are created at every round trip, and eventually a frequency comb forms. The optical power in the qth comb line is

$$P_q \propto \mathrm{e}^{-|q|\frac{2\pi f_o}{Q\,\mathrm{FSR}\,|\phi_r|}}, \tag{1}$$

where Q is the quality factor of the optical cavity and $|\phi_r|$ is the electro-optical phase shift acquired over an optical round-trip.[12] The latter is often expressed as $\pi V/V_\pi$ with the voltage V applied by the source and the half-wave voltage V_π that characterizes the modulator.

The conversion efficiency of the pump to the comb lines is key for reducing power consumption and increasing the comb span. On the one hand, this can be achieved by improving the quality factor Q of the optical resonator, for example, by reducing the optical

propagation losses[13] or by using wider waveguides that support multiple modes.[14] As an alternative, the resonator can be operated in the under-coupled regime, which, however, penalizes the output comb power. Recently, mutually coupled resonators have been shown to increase the conversion efficiency by up to 30% and consequently increase the EO comb bandwidth.[15]

On the other hand, the interaction between microwaves and optical fields, captured by $|\phi_r|$, is equally important for increasing the conversion efficiency. The behavior of the interaction depends on whether the modulator is in a traveling or standing wave configuration. For modulators operating in a traveling wave configuration, the microwaves and optical waves co-propagate, as in early demonstrations with fiber cavities. Then, the accumulated phase shift $|\phi_r|$ is clearly maximum if the velocities of the microwave and optical wave packets are matched [see Fig. 1(a)]. The tight integration of optical and microwave circuits in PICs enabled the investigation of different electrode designs and EO couplings, as recently shown by the use of resonant microwave cavities in lithium tantalate PICs.[16] Indeed, contrary to fiber-based EO combs, PIC-based devices can be and usually are designed such that the microwave is reflected and forms standing waves along the electrodes. In this case, the optical wave packet travels through a standing wave with nodes and antinodes in the voltage distribution [see Fig. 1(b)]. Therefore, the local electro-optic phase shift non-trivially varies in space and time. In turn, the accumulated phase shift $|\phi_r|$ and also the comb bandwidth show a non-trivial dependence on the electrode length, microwave feeding point, and modulation order $k = f_m/\mathrm{FSR}$.

In this paper, we present a flexible simulation method to predict the electro-optical phase shift for traveling and resonant configurations. The model only requires parameters (microwave losses, microwave index, and characteristic impedance) that can be either simulated from the cross section of the waveguide or extracted from measurements. With the model, we study the behavior of three different microwave configurations, and for each configuration, we vary electrode length and modulation order. We focus on a symmetric (A) and non-symmetric (B) resonant configuration and a traveling wave configuration (C), shown in the top row of Fig. 2. In addition, we validated the model with electro-optical measurements.

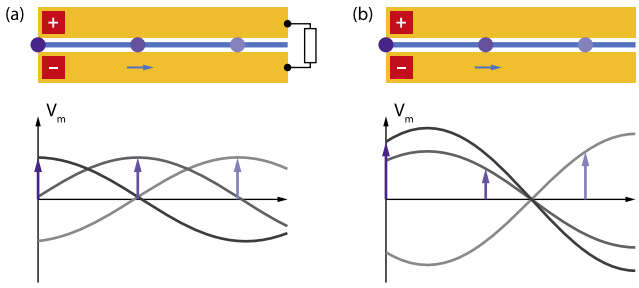

FIG. 1. Interaction between microwaves and optical fields. (a) In traveling wave operation, the microwaves propagate without backreflections from the injection location (red squares) along the electrodes (yellow) to the matched termination. The optical wave packet travels with equal speed along the waveguide (blue line), and the violet circles indicate three snapshots. The traveling voltage waves V_m are shown at these snapshots (gray curves). The voltage that the wave packet experiences is indicated by violet arrows in the distributions. (b) In standing wave operation, the microwaves are reflected at the open termination, leading to a standing voltage wave V_m along the electrodes. The snapshots are indicated at the same times as in panel (a).

II. THEORETICAL MODEL

Our model relies on transmission line theory to predict the voltage experienced by a wave packet for a given electrical configuration. Through the Pockels effect, this voltage leads to a local electro-optic phase shift. After integrating the local phase shifts over an optical round trip, we obtain the accumulated phase shift ϕ_r.

We first abstract the schematics (top row) into equivalent electrical circuits (bottom row) as depicted in Fig. 2. The devices are composed of individual modulation segments, each consisting of a microwave transmission line (in gray) and an optical waveguide (in blue); the inner pads connecting these segments can be neglected due to an up–down symmetry. The segments are driven by a microwave source with open-circuit voltage V_0 and internal resistance Z_S of 50 Ω.

The electro-optic phase shifts of the individual segments add up to the total shift,

$$\phi_r(t_0) = \sum_j \phi_j(t_j), \tag{2}$$

where ϕ_j denotes the shift in the jth segment and t_j the time when the wave packet enters this segment. The individual phase shifts depend on whether the wave packet enters the segment from the microwave source (s) or load (l) side (Appendix A extending Ref. 17). In a normalized form, they are

$$\frac{\phi_s(t_j)}{\phi_{\mathrm{norm}}} = -\sigma \frac{L_e}{L_r^{\min}} \mathrm{e}^{\mathrm{i}\omega_m t_j} \left[\frac{V^+}{V_0} F(u_s^+) + \frac{V^-}{V_0} F(u_s^-) \right], \tag{3}$$

$$\frac{\phi_l(t_j)}{\phi_{\mathrm{norm}}} = -\sigma \frac{L_e}{L_r^{\min}} \mathrm{e}^{\mathrm{i}\omega_m t_j} \mathrm{e}^{2\pi \mathrm{i} L_e/L_r^{\min}} \left[\frac{V^+}{V_0} F(u_l^+) + \frac{V^-}{V_0} F(u_l^-) \right]. \tag{4}$$

The parameter σ takes the value +1 for parallel and −1 for antiparallel orientation of the positive voltage direction (red squares in Fig. 2) with respect to the crystal axis (axis e in Fig. 2). The length L_e of the electrodes is normalized with the length $L_r^{\min} = v_o/f_m$, which is the shortest possible length of the optical ring, i.e., a ring with FSR = f_m, ($k = 1$). The voltages $V^\pm$ are amplitudes of the two waves traveling in opposing directions on the segment and implicitly depend on transmission line parameters, namely, the linear attenuation constant α_m, the phase velocity v_m, and the characteristic impedance Z_0. These parameters depend on the material and the geometry of the cross section, which are the same for all modulation segments. The amplitudes $V^\pm$ can be computed from the electrical configuration in a cascaded manner, as shown in Appendix B. The function $F(u)$ is given by $F(u) = (1 - \mathrm{e}^u)/u$ with dimensionless arguments,

$$u_s^\pm = \left[2\pi \mathrm{i} \left(1 \mp \frac{n_m}{n_o} \right) \mp \alpha_m L_r^{\min} \right] \frac{L_e}{L_r^{\min}}, \tag{5}$$

$$u_l^\pm = \left[2\pi \mathrm{i} \left(-1 \mp \frac{n_m}{n_o} \right) \mp \alpha_m L_r^{\min} \right] \frac{L_e}{L_r^{\min}}, \tag{6}$$

where $n_m = c/v_m$ and $n_o = c/v_o$ are the microwave phase index and optical group index, respectively.[18,19] The term ϕ_{norm} corresponds to

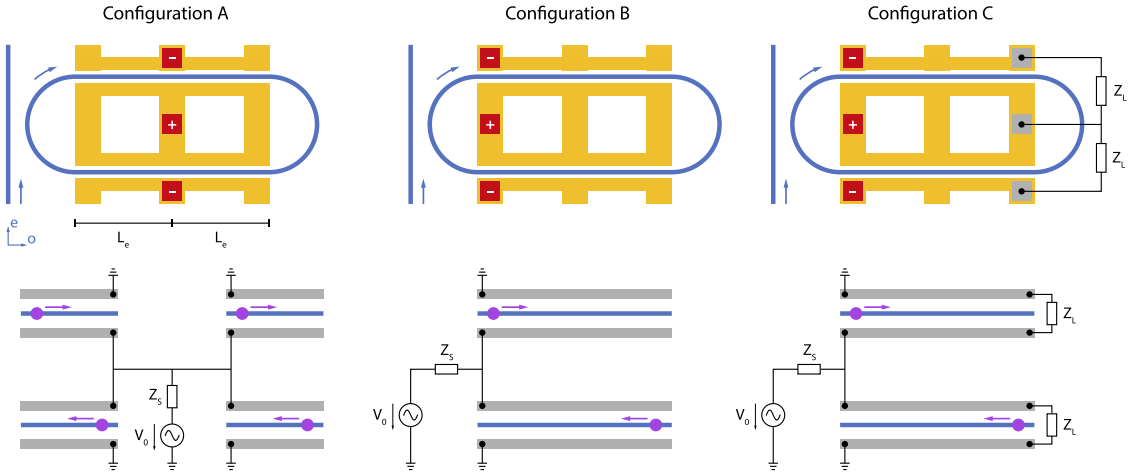

FIG. 2. Studied configurations of microcombs. Top row: Schematics of devices consisting of optical ring resonators and bus waveguides (blue) and microwave electrodes (yellow) with different terminations. Microwaves are injected into the device at the locations marked by the red squares, with the signs defining the positive electrical polarity. In configurations A and B, the electrodes are open at their ends (resonant modulator), and in configuration C, the electrodes are terminated with a matched load ($Z_L = Z_0$) and source ($Z_S = Z_0/2$) (traveling modulator). The extraordinary (e) and ordinary (o) axes of TFLN are indicated as coordinate axes. Bottom row: Equivalent circuits with a microwave source (open-circuit voltage V_0, internal impedance $Z_S = 50\ \Omega$) and modulation segments made up of optical waveguides (blue) and microwave transmission lines (gray). All transmission lines have the same characteristic impedance Z_0, linear attenuation constant α_m, and microwave index n_m.

the phase shift that would be induced by a modulator of length $L_r^{\min}$ with constant voltage V_0,

$$\phi_{\text{norm}} = \frac{\pi n_r^3 r}{\lambda_o} \frac{\Gamma L_r^{\min}}{G} V_0, \tag{7}$$

where n_r is the refractive index of the active medium without a microwave field, r the Pockels coefficient, λ_o the vacuum wavelength of light, and G the gap between the electrodes. The factor Γ is the normalized overlap between the optical mode E_o and the microwave field E_m and considers the inhomogeneity of the fields over the cross section,

$$\Gamma = \frac{G}{V} \frac{\iint_A |E_o(\mathbf{r})|^2 E_m(\mathbf{r})\, dS}{\iint_S |E_o(\mathbf{r})|^2\, dS}, \tag{8}$$

where V denotes the voltage between the electrodes and the integral in the numerator (denominator) runs over the active region A (entire cross section S).

The model presented in Eqs. (2)–(7) allows us to compute the phase shift $|\phi_r|$. The half-wave voltage V_π can be retrieved for any modulation scheme by imposing $|\phi_r| = \pi$. Although the model contains many parameters, only a few unitless quantities determine the normalized round-trip phase shift $|\phi_r|/\phi_{\text{norm}}$. Namely, the ratio of electrode and shortest ring length $L_e/L_r^{\min}$, the ratio of microwave and optical indices n_m/n_o, the dimensionless microwave losses $\alpha_m L_r^{\min}$, the order of the modulation $k = f_m/\text{FSR}$, and the ratio of characteristic and source impedances Z_0/Z_S. The parametrization of configuration C requires an additional unitless ratio, the normalized load impedance Z_L/Z_S.[20]

III. MODEL APPLICATION

Equipped with the theoretical model (Sec. II), we study the behavior of the configurations A, B, and C depicted in Fig. 2 in two scenarios. In the first scenario, we keep the open-circuit voltage V_0 constant since the induced electro-optical phase shift is proportional to voltage. Then, different configurations may consume different amounts of microwave power. Therefore, in the second scenario, we hold the total dissipated microwave power P_{tot} fixed.

A. Constant open-circuit voltage

We first analyze the behavior of the phase shift $|\phi_r|$ and then discuss its implications for the bandwidth of the optical comb.

Figure 3 shows the simulated $|\phi_r|$ vs electrode length L_e in normalized forms for different modulation orders k. We interpret the normalized electrode length $4L_e/L_r^{\min}$ using the ring length $L_r = v_o/\text{FSR}$ and relate it to $L_r^{\min}$ as $L_r = kL_r^{\min}$. Therefore, the normalized electrode length is expressed through the electrode coverage $4L_e/L_r$ as $4L_e/L_r^{\min} = k(4L_e/L_r)$. Since the electrode coverage assumes values from zero to one, the normalized electrode length varies from zero to k. Note that each panel in Fig. 3 includes one phase shift curve for each modulation order k. However, the curves overlap for all odd (solid lines) and separately for all even (dotted lines) modulation orders, and each one stops at the corresponding integer k. For example, for $k = 5$, the related solid line only exists in the gray area. For a physical device with fixed electrode coverage $4L_e/L_r$ of 80%, the normalized electrode length $4L_e/L_r^{\min}$ is 4. If by changing the modulation frequency, the modulation order is reduced to $k = 3$, the normalized electrode length will be 2.4.

Figure 3(a) shows the simplified case without microwave losses ($\alpha_m = 0$) and with matched microwave and optical velocities ($n_m = n_o$). In configuration A, the modulation oscillates up and

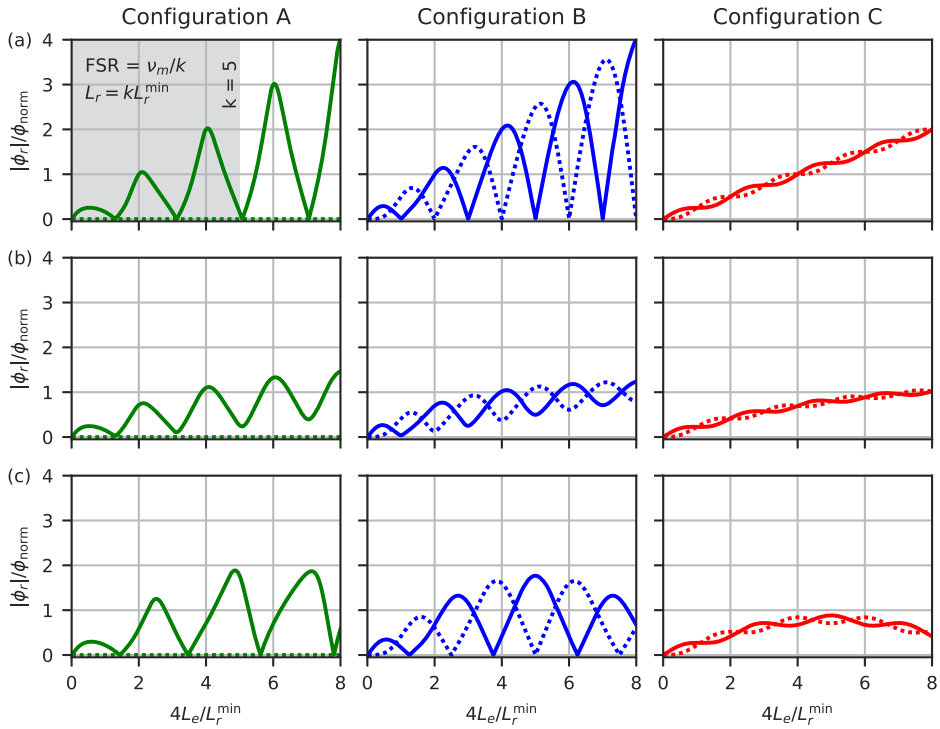

FIG. 3. Electro-optical phase shift at constant voltage V_0. Simulated phase shift $|\phi_r|$ vs electrode length L_e in normalized form for odd (solid line) and even (dashed line) modulation order $k = f_m/\text{FSR}$. The ratio $4L_e/L_r^{\min}$ can assume values from zero to the order of modulation k (e.g., a gray area for $k = 5$). Prediction for a case (a) without microwave losses ($\alpha_m = 0$) and with velocity matching ($n_m = n_o$), (b) with microwave losses ($\alpha_m L_r^{\min} = 0.39$) and velocity matching, and (c) with velocity mismatch ($n_m/n_o = 0.8$) and without microwave losses. All simulations use a characteristic impedance $Z_0 = 2Z_S$ and a load impedance $Z_L = 2Z_S$ for configuration C.

down as a function of the electrode length for odd modulation orders, as a consequence of the standing microwave pattern. Starting from the second maximum, the maxima of the electro-optical phase shift increase linearly with electrode length. This is because, when moving to the next maximum, the standing wave in each of the four electrodes extends by $\lambda_m/2$, adding a constant contribution to the electro-optic phase shift. Conversely, for even modulation orders, the total phase shift vanishes due to an inversion symmetry of the structure; the local phase contributions that are shifted by half a round-trip compensate each other. For configuration B, the electro-optic phase shift also oscillates with electrode length, and the maxima are increasing linearly. However, in contrast to configuration A, the inversion symmetry is absent, leading to a non-zero electro-optical phase shift for both even and odd modulation orders. In the traveling wave configuration C, the phase shift swings about a linear increase vs electrode length. The linear increase is caused by the upper electrodes, where optical wave packets and microwaves co-propagate with the same velocities. The small oscillations are produced by the lower electrodes in which the two waves propagate in opposite directions.

Figure 3(b) depicts the situation when introducing microwave losses ($\alpha_m \neq 0$). Microwave losses clearly decrease the phase shift, since they exponentially damp the voltage waves along the electrodes. Configuration A is less sensitive to losses than B and C, since the distance from the injection point to the electrode end is shorter. In addition, the decrease in modulation is stronger for longer electrodes, leading to saturation.

In Fig. 3(c), we introduce a velocity mismatch ($n_m \neq n_o$) and keep the microwave losses zero. In configuration C, the velocity mismatch mainly reduces the phase shift ϕ_r, since the lag between the evolutions accumulates in the upper electrodes. The contribution of the lower electrodes can slightly increase or decrease depending on the mismatch. Interestingly, for the resonant configurations A and B, the phase shift can increase compared to the case with matched velocities if the microwave is slightly faster than the optical evolution. Indeed, in Fig. 3(c), the maximal phase shifts are increased for the first few peaks. This is because, when increasing the phase velocity v_m of the microwaves, the period $\lambda_m = v_m/f_m$ of the standing wave increases and, therefore, also the electrode lengths at which the phase shift is maximal. Since the maxima are shifted toward longer electrode lengths, the first few peaks assume higher phase shifts. However, for the following peaks, the timing mismatch between the wave packet and the standing wave dominates and reduces the peak height.

According to Eq. (1), the bandwidth of the optical comb reads $\eta = Q\,\text{FSR}|\phi_r|/2\pi f_o$. We normalize the optical bandwidth η to factor out all k-independent quantities,

$$\frac{\eta}{\eta_{\text{norm}}} = \frac{1}{k}\frac{|\phi_r|}{\phi_{\text{norm}}}, \tag{9}$$

$$\eta_{\text{norm}} = \frac{n_r^3 r\Gamma}{G}\frac{QV_0}{n_o}. \tag{10}$$

Physically, the bandwidth η_{norm} is achieved with an electro-optical phase shift ϕ_{norm} and first modulation order k.

Figure 4 shows the optical bandwidth η vs electrode length L_e in normalized form for the simplified case ($\alpha_m = 0$ and $n_m = n_o$). In configuration C, the optical bandwidth saturates to a value that is independent of the modulation order k. The linearly increasing

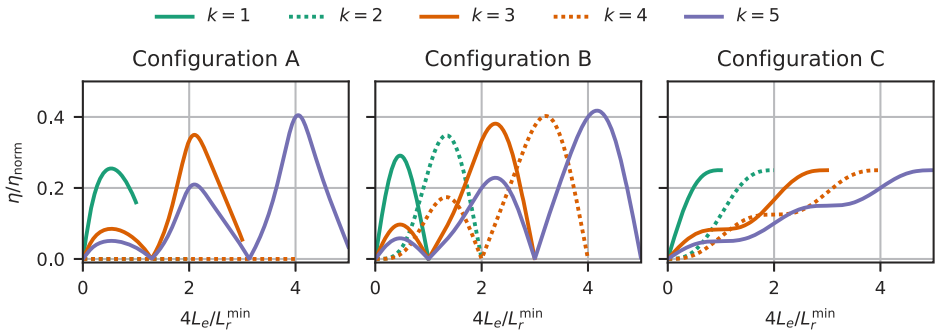

FIG. 4. Optical bandwidth for configurations A, B, and C at constant voltage V_0. Simulated optical bandwidth η vs electrode length L_e in normalized forms for different modulation orders k. Curves are the predictions without microwave losses ($\alpha_m = 0$) and with matched velocities ($n_m = n_o$). All simulations use a characteristic impedance $Z_0 = 2Z_S$ and a load impedance $Z_L = 2Z_S$ for configuration C.

phase shift with electrode length in Fig. 3(a) is compensated by the higher modulation order in the denominator of Eq. (9). Introducing microwave losses ($\alpha_m \neq 0$) or velocity mismatches ($n_m \neq n_o$) strongly reduces the electro-optical phase shift and, therefore, also the optical bandwidth for longer electrodes. Therefore, it is beneficial to use configuration C always with the first modulation order. For configurations A and B, the optical bandwidth can be increased for higher modulation orders in the simplified case. Adding microwave losses reduces the electro-optic phase shift, especially for longer electrodes and, therefore, causes the same reduction in the optical bandwidth. As a consequence, the higher the microwave losses, the lower the modulation order, which maximizes the bandwidth. Introducing moderate velocity mismatch ($n_m < n_o$) increases the optical bandwidth due to the same behavior of the phase shift in Fig. 3(c).

B. Constant dissipated power

Here, we compare the configurations A, B, and C when the total microwave power dissipated in the source and structure is fixed. Based on the equivalent circuits at the bottom of Fig. 2, the dissipated microwave power is $P_{\text{tot}} = \text{Re}(V_0 I_0^*/2)$ with the open-circuit voltage V_0 and the current I_0 provided by the source. The current I_0 can be expressed as $V_0/(Z_S + Z_1)$ with the impedance Z_1 of the structure as calculated in Appendix B [Fig. 10(b)]. Therefore, the total dissipated power is

$$P_{\text{tot}} = \frac{1}{2}\frac{\text{Re}(Z_S + Z_1)}{|Z_S + Z_1|^2}|V_0|^2. \tag{11}$$

Since the impedance Z_1 generally depends on the configuration and the electrode length, the voltage V_0 needs to vary accordingly to keep the dissipated power constant.

Figure 5 shows the phase shift $|\phi_r|$ vs electrode length $4L_e/L_r^{\text{min}}$ with fixed dissipated power. Since the ϕ_{norm} normalizes V_0 from the phase shift, we explicitly multiply $\phi_r/\phi_{\text{norm}}$ by V_0 to ensure that the dissipated power is constant for all electrode lengths [see Eq. (11)]. To keep V_0 always finite, we require microwave losses in the electrodes ($\alpha_m \neq 0$). The curves in dark colors are simulated for the same microwave losses as in Fig. 3(b), while the lighter curves have five times lower losses.

Since in configuration C the electrodes and loads are matched, the impedance Z_1 and, therefore, also the voltage V_0 are independent of the electrode length. We choose a dissipated power $P_{\text{tot}} = 5$ mW such that the voltage $V_0 = 1$ V. Therefore, the dark red curves are identical to those in Fig. 3(b). For lower microwave losses (light red curves), the phase shifts are larger.

In configurations A and B, the electrodes are open and, therefore, the voltage V_0 varies with electrode length. The voltage and, therefore, also the phase shift are particularly high at the parallel resonances of the structure when the impedance Z_1 is real and large. This happens for even ratios ($4L_e/L_r^{\text{min}}$ for configuration A) and integer ratios for configuration B. The peak phase shifts are larger for lower microwave losses and are only limited by the ability of the power supply to deliver high voltages. The resonant configurations A and B only dissipate in the electrodes, while configuration C additionally dissipates in the terminations. Therefore, at fixed dissipated

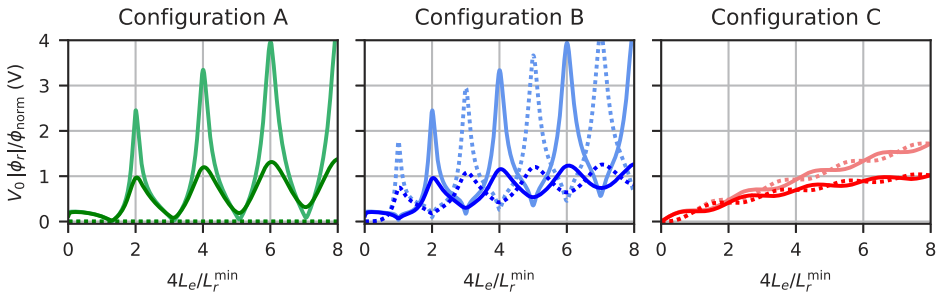

FIG. 5. Electro-optical phase shift at constant dissipated power. Simulated phase shift vs normalized electrode length for odd (solid line) and even (dashed line) modulation order $k = f_m/\text{FSR}$. The normalized microwave losses $\alpha_m L_r^{\text{min}}$ are 0.39 for dark-colored curves and 0.077 for light-colored curves. For all simulations, the velocities are matched ($n_m = n_o$), the source impedance Z_S is 50 Ω, the characteristic impedance $Z_0 = 2Z_S$, and the load impedance $Z_L = 2Z_S$ for configuration C. The total dissipated power P_{tot} is fixed to 5 mW.

power, the phase shifts, and hence also the optical bandwidths, can be substantially higher in the resonant configurations.

IV. EXPERIMENTAL VALIDATION

In order to experimentally validate our model, we have fabricated and characterized EO microcombs based on TFLN.

A. Fabrication of microcombs

Figure 6(a) shows five fabricated microcombs with microwave electrodes and optical waveguides as schematically depicted in Fig. 2. The contacts for microwave excitation are clearly visible. The five microcombs differ in their electrode lengths; from left to right, the electrode coverages $4L_e/L_r$ are 80%, 68%, 56%, 44%, and 32%. The microrings have a FSR of 40.3 GHz. For each electrode length, microcombs with five different point coupling gaps between bus waveguides and microrings have been fabricated at ETHZ from a commercially available x-cut wafer (NANOLN). The film thickness of the lithium niobate is 600 nm on a 4.7 μm buried oxide layer. Circuits are patterned using electron beam lithography on a 650 nm thick hydrogen silsesquioxane resist, and the waveguides are subsequently etched in an inductively coupled-plasma reactive-ion-etching system using Ar^+ ions. The target etch depth is 300 nm and is ensured by using an interferometric endpointing technique. The material redeposited during etching is then removed using a potassium hydroxide solution while the residual mask is etched with a short dip into buffered hydrofluoric acid. Samples are then annealed at 500 °C for 2 h in order to heal damages from fabrication, thus lowering propagation losses. The fabrication process of the waveguides is thoroughly described in Ref. 21. Electrodes are deposited by the liftoff process of gold and patterned using a double-layer polymethyl methacrylate resist stack; the target metal thickness is 500 nm, and 5 nm of chromium are used to improve adhesion to lithium niobate. PICs are then diced and mechanically polished to improve the end-fire coupling efficiency. To further validate the model in a wafer-scale process, a new set of rings with a smaller FSR of 14.2 GHz has been fabricated at CSEM in a multi-project wafer run (foundry service https://www.csem.ch/en/tailored-services/tfln-foundry-services). In this case, the waveguides are patterned by etching 400 nm out of a 600 nm-thick x-cut lithium niobate wafer by an optimized ion milling technology. A silicon oxide cladding is used to protect the chip surface. Then, the cladding is selectively removed in the desired area to grant access to the metal contacts.

B. Characterization of microcombs

The experimental setup in Fig. 6(b) is used to generate and characterize the optical combs. A continuous-wave tunable laser

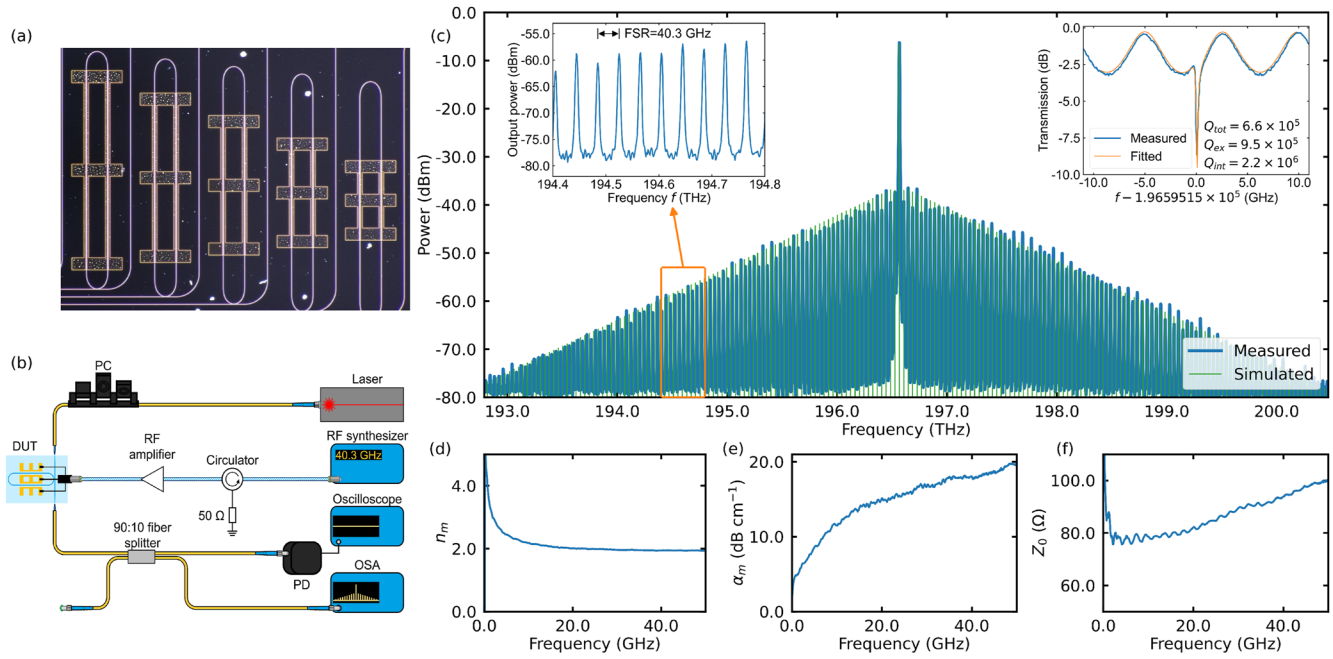

FIG. 6. Microcombs, experimental setup, and characterization. (a) Optical image of fabricated microcombs with different electrode lengths and the same FSR. (From Volpini *et al.*, *CLEO/Europe-EQEC*. Copyright 2025 IEEE. Reproduced with permission from IEEE.)[22] (b) Experimental setup for characterizing the microcombs (DUT). Laser light is conditioned with a polarization controller (PC) and then pumps the DUT. The light from the DUT is analyzed with an optical spectrum analyzer (OSA) and a photodetector (PD). The microwaves are generated by an RF synthesizer, boosted by an amplifier and then injected into the DUT. A circulator protects the synthesizer from reflected microwaves. (c) Example of a frequency comb measured with the OSA and a zoom onto a few comb lines (left inset). Right inset: Transmission spectrum of the ring taken at low optical power without microwave modulation. (From Volpini *et al.*, *CLEO/Europe-EQEC*. Copyright 2025 IEEE. Reproduced with permission from IEEE.)[22] (d)–(f) Transmission line parameters extracted from a measurement with a vector network analyzer (VNA), namely (d) effective microwave index n_m, (e) linear attenuation constant α_m, and (f) characteristic impedance Z_0 as a function of the microwave frequency.

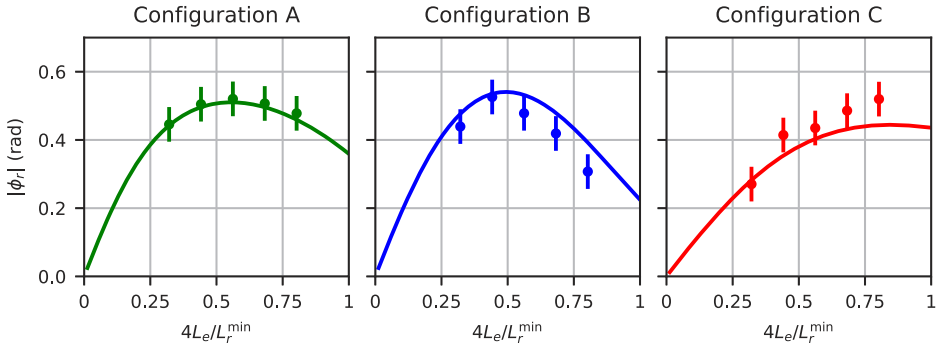

FIG. 7. Validation of the theoretical model with the first modulation order. Electro-optical phase shift $|\phi_r|$ vs normalized electrode length $4L_e/L_r^{\min}$ with equal modulation frequency and free spectral range of 40 GHz for configurations A, B, and C. The measured and simulated phase shifts are indicated as points and curves, respectively. The measured values (uncertainties) correspond to means (standard deviations) for modulators with varying gaps between ring and bus waveguides. The simulations only contain the source voltage V_0 as a global scaling factor, which is fitted to all measurements simultaneously. All other parameters are determined independently. The optical group index n_o is 2.3, the characteristic impedance Z_0 is 93.8 Ω, the microwave effective index n_m is 1.9, the linear attenuation constant α_m is 206 Np m^{-1} (17.9 dB cm^{-1}), the source impedance Z_S is 50 Ω, and the load impedance Z_L is 100 Ω for configuration C.

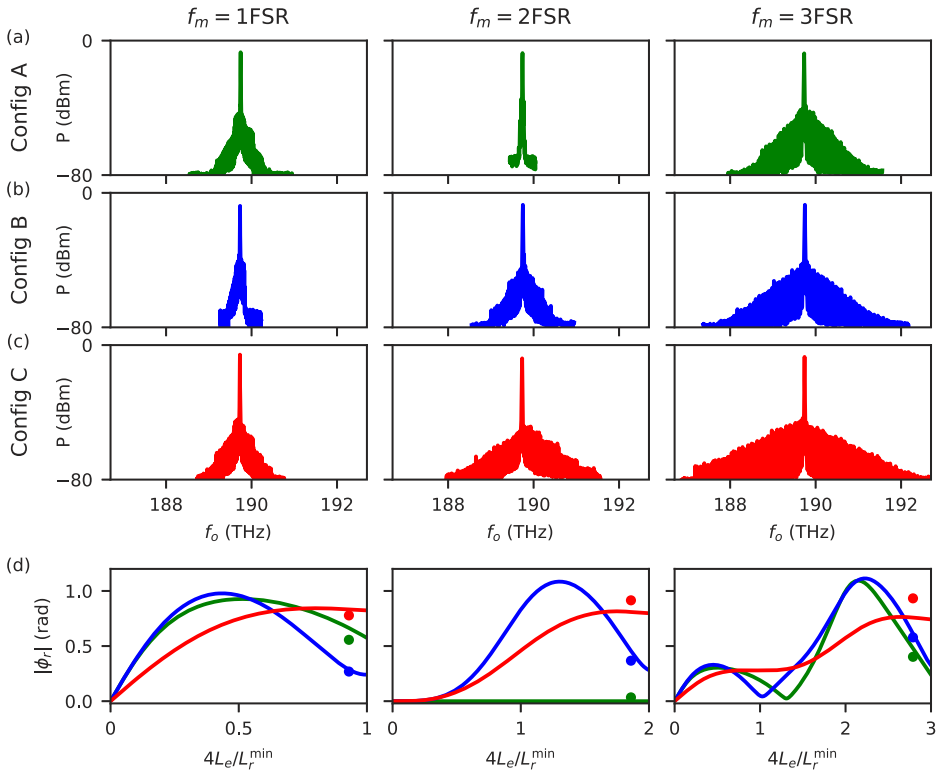

FIG. 8. Validation of the theoretical model with higher modulation orders. Measured optical power P vs optical frequency f_o at three modulation frequencies f_m of 1FSR, 2FSR, and 3FSR for (a) configuration A (green), (b) configuration B (blue), and (c) configuration C (red). The used modulator has a free spectral range (FSR) of 14.219 GHz. (d) Simulated (curves) and measured (dots) electro-optical phase shift $|\phi_r|$ vs normalized electrode length $4L_e/L_r^{\min}$ for the corresponding modulation frequencies (columns) and configurations (colors). The simulations only contain the source voltage V_0 as a global scaling factor, which is fitted to all measurements simultaneously. All other parameters are determined independently. The optical group index n_o is 2.28, the source impedance Z_S is 50 Ω, and the load impedance Z_L is 100 Ω for configuration C. The transmission line parameters depend on the modulation frequencies of 1FSR, 2FSR, and 3FSR: The characteristic impedances Z_0 are 93.2, 92.0, and 85.5 Ω; the microwave effective indices n_m are 2.3, 2.2, and 2.2; the linear attenuation constants α_m are 70.8 Np m^{-1} (6.2 dB cm^{-1}), 84.3 Np m^{-1} (7.3 dB cm^{-1}), and 91.9 Np m^{-1} (8.0 dB cm^{-1}).

(TOPTICA CTL 1550) is coupled to the quasi-TE mode of the chip with a lensed fiber and a polarization controller (PC). The output signal is also collected with a lensed fiber, and it is split using a 90:10 fiber coupler; 10% of the laser power is sent to a photodiode (PD), which is used for chip alignment, while 90% of the output is measured by an optical spectrum analyzer (OSA). The microwave driving signal is generated by an RF synthesizer (Keysight E8257D) and then amplified and directed to an RF circulator. One output of the circulator is connected to the microwave ground-signal-ground probe, which drives the electrodes of the microcomb. The microwave power, which is back-reflected from the sample, enters the circulator and is dissipated into a 50 Ω termination.[23,24] When operating the microcombs in configuration C shown in Fig. 2, we added a second microwave probe with a 50 Ω termination to the other end of the electrode.

Figure 6(c) depicts an example of an EO comb spectrum. The experimental values of $|\phi_r|$ are obtained with Eq. (1). For this, the logarithm of the measured power in each comb line is fitted by a linear function. The Q factor is extracted from the optical transmission spectra of the microcombs without microwave excitation (see right inset). The FSR is extracted from the transmission spectrum and also from optimizing the comb bandwidth by fine-tuning the applied microwave frequency.

In addition, we measured the transmission line parameters such as microwave index n_m, propagation losses α_m, and characteristic impedance Z_0 [Figs. 6(d)–6(f)], and we use them as model parameters. They are extracted from the scattering matrices obtained with a vector network analyzer (Rohde & Schwarz ZNA) as explained in Appendix C.

C. Validation of theoretical model

We validated the theoretical model for the configurations A, B, and C with two experiments. In the first experiment, we extracted the phase $|\phi_r|$ of the samples fabricated at ETHZ, featuring structures with different electrode lengths and identical FSR. The modulation is performed at the first order with $f_m = 40.3$ GHz. Figure 7 demonstrates a good agreement between measured and simulated $|\phi_r|$ as a function of the electrode length. Remarkably, the model contains only a single free fitting parameter, the source voltage V_0, which simultaneously scales the phase shift for all configurations. All other parameters are determined independently: the transmission line parameters are separately measured as described in Sec. IV B, while the optical group index is obtained from the cross section using an electromagnetic solver. Configuration A and B reach their maxima at similar electrode lengths, while in configuration C, the maximum is shifted to longer electrodes.

In the second experiment, we validated the model at higher modulation orders. For this, we used a sample fabricated at CSEM with an electrode coverage $4L_e/L_r$ of 93% and a smaller FSR of 14.2 GHz. By changing the microwave frequency f_m to 1FSR, 2FSR, and 3FSR, we reached the first three modulation orders k. Figure 8 displays the measured frequency combs for the three modulation orders. In configuration A, the modulation vanishes for $k = 2$, as a consequence of the inversion symmetry of the structure (Sec. III), leading to a very narrow frequency comb. This suppression is absent for configurations B and C. The precise dependence of $|\phi_r|$ on the electrode length for different excitation orders can be predicted with the theoretical model, and it is shown in Fig. 8(d). The same panel also reports the extracted $|\phi_r|$ from the experimentally generated combs reported in Fig. 8(a)–8(c), and it displays a good agreement between theory and measurement.

V. DISCUSSION AND CONCLUSION

We have developed an analytical model that can predict the strength of the electro-optical phase modulation and, therefore, the optical bandwidth, for resonant microcombs with generic microwave configurations. It requires input parameters for the microwave and optical waveguides, which can be easily accessed through measurements or simulations.

To validate the approach, we have fabricated and characterized ring modulators with three different electrode configurations: standing microwaves with central (A) and side (B) feeding and traveling microwaves with side feeding (C). For each configuration, we have also explored the advantage of driving the microcomb at a higher modulation order when the microwave frequency f_m is a multiple k of the optical FSR.

We found that in standing wave configurations, the bandwidth of the microcomb strongly depends on the electrode length and can even go to zero. Interestingly, contrary to traveling wave excitations and to non-resonant EO modulators, the largest phase shift is not achieved when maximizing the electrode length. As an example, we compute gains in modulation efficiency using values commonly reported in the literature.[25] When the electrodes are shortened from the longest to the optimal length provided by the model, the gains are 29% for configuration A and 104% for configuration B, while for configuration C, the longest electrodes are already the most efficient. However, with properly optimized electrode lengths and modulation orders, the optical bandwidth is always larger in standing wave compared to traveling wave operation.

In addition, for standing wave configurations, higher modulation orders yield larger optimal bandwidths in an ideal lossless case with matched velocities. However, in non-ideal cases, this increase stops at a certain modulation order and then reverts due to the need for longer electrodes and microrings. This means that, in practice, moderate modulation orders are optimal for achieving maximal bandwidth. Interestingly, if the modulation order is fixed, the bandwidth can be increased by making the microwave slightly faster than the optical wave packet.

These findings help to optimize the optical bandwidth in PIC-based microcombs under constraints dictated by chip layout, excitation scheme, modulation frequency, etc. In addition, it provides guidelines for the chip design. For instance, the optimal electrode length is shorter in standing-wave than in traveling-wave configurations at the same modulation order. This feature can be exploited to increase the bending radius of the optical cavity, increasing the optical quality factor and, hence, the comb bandwidth. In addition, if a single access point for microwaves is required, the studied standing wave configurations are useful with either feeding on one side (configuration B) or in the middle (configuration A). Since they have similar performances, the more flexible excitation scheme from the side can be chosen.

In general, this model is valuable for predicting the behavior of electro-optic components, in which non-trivial spatial and temporal variations of the microwave fields are relevant during the optical

evolution. The method can be equally applied to traveling, standing wave, and RF resonant modulators integrated in a microwave network. The implementation in Python is available as an open-source package: https://github.com/samuehae/electrooptic.

ACKNOWLEDGMENTS

This study was funded by the Swiss National Science Foundation (SNSF) with the BRIDGE Project No. 194693.

AUTHOR DECLARATIONS

Conflict of Interest

The authors have no conflicts to disclose.

Author Contributions

S. Häusler: Data curation (lead); Formal analysis (equal); Methodology (lead); Software (lead); Validation (equal); Visualization (lead); Writing – original draft (equal); Writing – review & editing (equal). **A. Volpini**: Formal analysis (equal); Validation (equal); Writing – original draft (equal); Writing – review & editing (equal). **G. Finco**: Resources (equal); Writing – original draft (supporting); Writing – review & editing (supporting). **G. Li**: Resources (supporting). **C. Caër**: Formal analysis (supporting); Visualization (equal); Writing – review & editing (equal). **J. S. Holzer**: Formal analysis (supporting). **H. Sattari**: Resources (equal). **H. Zarebidaki**: Resources (equal). **I. Prieto**: Resources (equal). **S. Lecomte**: Funding acquisition (equal). **R. Grange**: Conceptualization (supporting); Funding acquisition (equal); Resources (equal); Supervision (equal). **C. Wildfeuer**: Conceptualization (equal); Project administration (equal); Supervision (equal); Writing – review & editing (supporting). **D. Grassani**: Conceptualization (lead); Project administration (equal); Supervision (equal); Writing – original draft (equal); Writing – review & editing (equal).

DATA AVAILABILITY

The data that support the findings of this study are available from the corresponding authors upon reasonable request.

APPENDIX A: DERIVATION OF THE ELECTRO-OPTIC PHASE SHIFT

In this section, we derive the optical phase shift caused by a single modulation segment based on building blocks from Chap. 6 in Ref. 17. A segment consists of an optical waveguide and a microwave transmission line where the light enters the segment either (a) from the source or (b) from the load side, as shown in Fig. 9.

A first ingredient to calculate the optical phase shift is how the microwave (m) field behaves along the electrodes. The field is captured by voltage and current waves traveling in either direction within the transmission line theory.[26,27] Their superposition leads to the total voltage and current amplitudes in complex notation,[28]

$$V_m(x_m,t) = V^+ e^{i\omega_m t-\gamma_m x_m} + V^- e^{i\omega_m t+\gamma_m x_m}, \tag{A1}$$

$$I_m(x_m,t) = I^+ e^{i\omega_m t-\gamma_m x_m} + I^- e^{i\omega_m t+\gamma_m x_m}, \tag{A2}$$

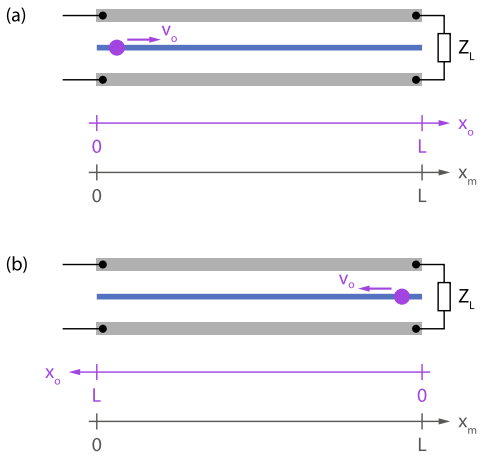

FIG. 9. Single modulation segment. A modulation segment consists of a microwave transmission line (gray) terminated with load Z_L and an optical waveguide (blue). A wave packet (purple circle) either travels (a) from source to load side or (b) vice versa. Coordinate systems with origins where light (x_o) or microwave (x_m) enters and with coordinate L on the other side.

with the angular microwave frequency ω_m, the propagation constant $\gamma_m = \alpha_m + i\beta_m$, combining the linear attenuation constant α_m and the phase constant β_m, and the complex voltage amplitudes $V^\pm$ and current amplitudes $I^\pm$. The amplitudes are connected by the characteristic impedance Z_0 as $I^\pm = \pm V^\pm/Z_0$. The fields are expressed in the coordinate x_m whose origin is located where the transmission line is excited (source side); therefore, the expressions are valid for both types of modulation segments in Fig. 9.

Next, we connect the local voltage V_m to the change in refractive index caused by the Pockels effect. The relation is given in Ref. 17 and reads

$$\delta n(x_o,t) = -\sigma \frac{n_r^3 r \Gamma}{2G} V_m(x_m,t), \tag{A3}$$

where σ includes the orientation of the crystal axis relative to the positive voltage direction (parallel: $\sigma = +1$, anti-parallel: $\sigma = -1$), n_r is the refractive index of the active medium without a microwave field, r denotes the Pockels coefficient, and G is the gap between the electrodes. Here, we introduced the coordinate system x_o, which points along the propagation direction of the light; it is convenient to later integrate the index change δn along the motion of the light.

The previous equation also depends on the normalized mode overlap between the optical and microwave fields,

$$\Gamma = \frac{G}{V} \frac{\iint_A |E_o(\mathbf{r})|^2 E_m(\mathbf{r})\, dS}{\iint_S |E_o(\mathbf{r})|^2\, dS}, \tag{A4}$$

with the voltage V between the electrodes, the electric field component E_m of the static microwave field, and the field component E_o of the optical mode. The relevant component of the fields is determined by the significant Pockels coefficient. The integral in the numerator (denominator) runs over the active region A (entire cross section S).

From the index change δn formulated in Eq. (A3), we derive now the optical phase shift accumulated within the modulation segment. It follows by integrating the local phase shifts $-k_o\delta n$ seen by the wave packet along the path of propagation,

$$\phi(t_0) = -\int_0^L k_o \delta n\left(x_o, t_0 + \frac{x_o}{v_o}\right)\mathrm{d}x_o, \tag{A5}$$

with the optical wave vector $k_o = 2\pi/\lambda_o$. Time t and position x_o are connected by the speed v_o of the wave packet and the time t_0 when the wave packet enters the modulation segment. The relation is valid for either type of modulation segment (see Fig. 9). Inserting Eq. (A3) leads to

$$\phi(t_0) = \sigma\frac{\pi n_r^3 r}{\lambda_o}\frac{\Gamma}{G}\int_0^L V_m\left(x_m, t_0 + \frac{x_o}{v_o}\right)\mathrm{d}x_o. \tag{A6}$$

In order to perform the integral in Eq. (A6), we change the integration variable from x_o to x_m. As the variable change depends on the type of modulation segment (Fig. 9), we distinguish the two cases. When the wave packet enters the modulation segment from the source side $(x_m = x_o)$, we obtain the result

$$\phi_s(t_0) = \sigma\frac{\pi n_r^3 r}{\lambda_o}\frac{\Gamma}{G}\int_0^L V_m\left(x_m, t_0 + \frac{x_m}{v_o}\right)\mathrm{d}x_m, \tag{A7}$$

and analogously for the case from the load side $(x_m = L - x_o)$,

$$\phi_l(t_0) = -\sigma\frac{\pi n_r^3 r}{\lambda_o}\frac{\Gamma}{G}\int_L^0 V_m\left(x_m, t_0 + \frac{L}{v_o} - \frac{x_m}{v_o}\right)\mathrm{d}x_m. \tag{A8}$$

Before inserting the expression for the voltage V_m from Eq. (A1), we use the relation $V_m(x, t + \Delta t) = \exp(\mathrm{i}\omega_m\Delta t)V_m(x, t)$ to pull out factors from the integral that are independent of x_m, namely with $\Delta t = t_0$ and $\Delta t = t_0 + L/v_o$, respectively. Finally, the optical phase shifts read

$$\phi_s(t_0) = -\sigma\frac{\pi n_r^3 r}{\lambda_o}\frac{\Gamma L}{G}\mathrm{e}^{\mathrm{i}\omega_m t_0}\left[V^+F(u_s^+) + V^-F(u_s^-)\right], \tag{A9}$$

$$\phi_l(t_0) = -\sigma\frac{\pi n_r^3 r}{\lambda_o}\frac{\Gamma L}{G}\mathrm{e}^{\mathrm{i}\omega_m t_0}\mathrm{e}^{\mathrm{i}\beta_o L}\left[V^+F(u_l^+) + V^-F(u_l^-)\right]. \tag{A10}$$

Here, we introduced the function $F(u) = (1 - \mathrm{e}^u)/u$ and the unitless arguments

$$u_s^\pm = \mathrm{i}(\beta_o \mp \beta_m)L \mp \alpha_m L, \tag{A11}$$

$$u_l^\pm = \mathrm{i}(-\beta_o \mp \beta_m)L \mp \alpha_m L, \tag{A12}$$

with $\beta_o = \omega_m/v_o$ and $\beta_m = \omega_m/v_m$, where v_m denotes the phase velocity of the microwave. Note that β_o is not the wave vector of light because it involves the microwave frequency.

Overall, the formulas for the optical phase shifts ϕ_s and ϕ_l are very similar. They only differ by a global phase factor, which considers that the wave packet enters on opposite ends of the modulation segment and the different sign in front of β_o in Eqs. (A11) and (A12) due to the opposite propagation direction of the light.

APPENDIX B: DETERMINATION OF THE VOLTAGE DISTRIBUTION

Here, we explain a method to calculate the complex voltage amplitudes V^+ and V^- in each modulation segment, which are necessary to obtain the optical phase shifts in Eqs. (3) and (4). As the voltage amplitudes depend on the entire microwave circuit, we demonstrate the procedure with the example circuit in Fig. 10(a). The microwave source is attached to a network of transmission lines, where the lines are connected in parallel or in series to each other, and finally, every branch is terminated by a specific load impedance (e.g., Z_6 and Z_8). Note that each transmission line in the circuit can either modulate light or simply route microwaves.

The method relies on the fact that the voltage amplitudes V^+ and V^- are fully determined by the voltage V_{in} and current I_{in} at the input of the transmission line [see Eqs. (A1) and (A2)], or alternatively, by the input voltage V_{in} and the input impedance Z_{in} since $I_{\mathrm{in}} = V_{\mathrm{in}}/Z_{\mathrm{in}}$. As it is easiest to obtain Z_{in} and V_{in}, the method calculates first the latter quantity and then the former.

In the first stage, we calculate the input impedances of every transmission line from its load impedance. Note that load and input impedances generally differ, as the voltage and current amplitudes vary on transmission lines and, therefore, also their ratio, the impedance.

1. We start at the terminations of the network (e.g., Z_6 and Z_8). The transmission lines directly connected to the terminations transform the load impedance Z_L (e.g., Z_6) to the input impedance Z_{in} (e.g., Z_5),[27]

$$Z_{\mathrm{in}} = Z_0\frac{Z_L + Z_0\tanh(\gamma_m L)}{Z_0 + Z_L\tanh(\gamma_m L)}, \tag{B1}$$

   with the complex propagation constant $\gamma_m = \alpha_m + \mathrm{i}\beta_m$, the linear attenuation constant α_m, and the phase constant β_m.
2. When several transmission lines are connected in parallel, combine their input impedances (e.g., Z_5 and Z_7) by summing their reciprocal values, e.g., $Z_4^{-1} = Z_5^{-1} + Z_7^{-1}$. The resulting input impedance is the load impedance of the next transmission line. When the transmission lines are connected in series,

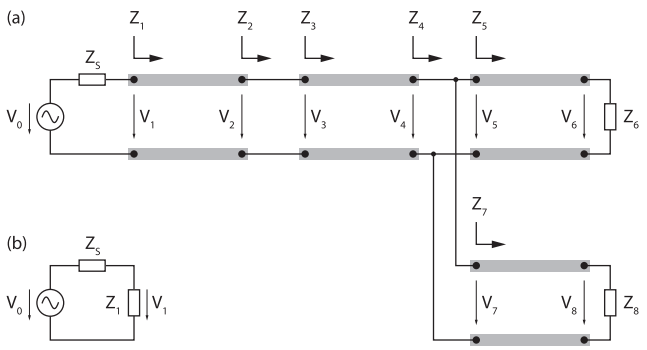

FIG. 10. Example of a microwave circuit. (a) A microwave source with open-circuit voltage V_0 and internal impedance Z_S is attached to a network of transmission lines (gray lines), which are either connected in series or in parallel to each other. The network is terminated with loads of impedance Z_6 and Z_8. (b) Equivalent circuit with load impedance Z_1 summarizing the terminated network.

then the input impedance is directly the load impedance of the next transmission line, e.g., $Z_2 = Z_3$.

3. We continue until the network simplifies to the schematic in Fig. 10(b).

Next, we calculate all the input voltages and with them the complex amplitudes V^+ and V^-:

1. In the first stage, we simplified the network to the equivalent circuit shown in Fig. 10(b). It is a voltage divider where the voltage V_1 is the input voltage of the first transmission line,

$$V_1 = \frac{Z_1}{Z_S + Z_1} V_0. \tag{B2}$$

2. From the input voltage V_{in} (e.g., V_1) and impedance Z_{in} (e.g., Z_1), we extract the voltage amplitudes V^+ and V^- on the (first) transmission line. The amplitudes follow from Eqs. (A1) and (A2) evaluated at the input location ($x_m = 0$) and starting time ($t = 0$),

$$V^+ + V^- = V_{\text{in}}, \tag{B3}$$

$$\frac{V^+}{Z_0} - \frac{V^-}{Z_0} = \frac{V_{\text{in}}}{Z_{\text{in}}}. \tag{B4}$$

We solve the equations for V^+ and V^- and obtain

$$V^+ = \frac{Z_{\text{in}} + Z_0}{2Z_{\text{in}}} V_{\text{in}}, \tag{B5}$$

$$V^- = \frac{Z_{\text{in}} - Z_0}{2Z_{\text{in}}} V_{\text{in}}. \tag{B6}$$

3. In order to propagate the voltage to the following transmission lines, we calculate the output voltage V_{out} (e.g., V_2) from the input voltage V_{in} (e.g., V_1). This is achieved by evaluating Eqs. (A1) and (A2) at the output location ($x_m = L$) and starting time ($t = 0$) with the voltage amplitudes obtained in the previous step,

$$V_{\text{out}} = V^+ \mathrm{e}^{-\gamma_m L} + V^- \mathrm{e}^{\gamma_m L}. \tag{B7}$$

The input voltage of the following transmission line(s), which are either connected in series or in parallel, is equal to the output voltage of the present transmission line (e.g., $V_3 = V_2$ or $V_5 = V_7 = V_4$).

Now, we can calculate the complex amplitudes V^+ and V^- on every transmission line.

APPENDIX C: EXTRACTION OF TRANSMISSION LINE PARAMETERS

Here, we describe the procedure used to determine the transmission line parameters. It starts with the scattering matrix S^{m} measured between the left and right pads of the structure in Fig. 2 and works as follows.

As the structure is symmetric, we first enforce symmetry ($S_{11} = S_{22}$ and $S_{12} = S_{21}$) on the measured scattering amplitudes by averaging the diagonal and off-diagonal elements separately and replacing the elements by the corresponding average. The average of the complex numbers is performed individually on magnitude and direction (Sec. II in Ref. 29).

The resulting scattering matrix $\bar{S}^m$ describes two identical transmission lines connected in parallel, as shown in Fig. 2. Therefore, we extract next the matrix $\bar{S}^l$ of a single transmission line. To this end, we first convert the scattering matrix $\bar{S}^m$ to the admittance matrix $\bar{Y}^m$ according to Ref. 30. As the lines are identical and connected in parallel, the admittance matrices are related by $\bar{Y}^m = 2\bar{Y}^l$ (Sec. II B 4 in Ref. 31). Therefore, we obtain the admittance matrix $\bar{Y}^l = \bar{Y}^m/2$ or, after conversion, the scattering matrix $\bar{S}^l$ of a single transmission line.

From the scattering matrix $\bar{S}^l$, we finally calculate the characteristic impedance Z_0, linear attenuation constant α_m, and effective microwave index n_m of a single transmission line according to the method proposed in Ref. 32 in Sec. II B. The numbers are stated in the main text.

REFERENCES

[1] E. L. Wooten, K. M. Kissa, A. Yi-Yan, E. J. Murphy, D. A. Lafaw, P. F. Hallemeier, D. Maack, D. V. Attanasio, D. J. Fritz, G. J. McBrien, and D. E. Bossi, "A review of lithium niobate modulators for fiber-optic communications systems," IEEE J. Sel. Top. Quantum Electron. **6**, 69–82 (2000).

[2] M. Kourogi, K. Nakagawa, and M. Ohtsu, "Wide-span optical frequency comb generator for accurate optical frequency difference measurement," IEEE J. Quantum Electron. **29**, 2693–2701 (1993).

[3] P. Rabiei and P. Gunter, "Optical and electro-optical properties of submicrometer lithium niobate slab waveguides prepared by crystal ion slicing and wafer bonding," Appl. Phys. Lett. **85**, 4603–4605 (2004).

[4] R. Takigawa and T. Asano, "Thin-film lithium niobate-on-insulator waveguides fabricated on silicon wafer by room-temperature bonding method with silicon nanoadhesive layer," Opt. Express **26**, 24413–24421 (2018).

[5] M. Zhang, C. Wang, R. Cheng, A. Shams-Ansari, and M. Lončar, "Monolithic ultra-high-q lithium niobate microring resonator," Optica **4**, 1536–1537 (2017).

[6] M. Yu, B. Desiatov, Y. Okawachi, A. L. Gaeta, and M. Lončar, "Coherent two-octave-spanning supercontinuum generation in lithium-niobate waveguides," Opt. Lett. **44**, 1222–1225 (2019).

[7] A. Shams-Ansari, M. Yu, Z. Chen, C. Reimer, M. Zhang, N. Picqué, and M. Lončar, "Thin-film lithium-niobate electro-optic platform for spectrally tailored dual-comb spectroscopy," Commun. Phys. **5**, 88 (2022).

[8] R. Niu, S. Wan, W. Li, P.-Y. Wang, F.-W. Sun, F. Bo, J. Liu, G.-C. Guo, and C.-H. Dong, "An integrated wavemeter based on fully-stabilized resonant electro-optic frequency comb," Commun. Phys. **6**, 329 (2023).

[9] Y. Okawachi, B. Y. Kim, M. Lipson, and A. L. Gaeta, "Chip-scale frequency combs for data communications in computing systems," Optica **10**, 977–995 (2023).

[10] K. Twayana, I. Rebolledo-Salgado, E. Deriushkina, J. Schröder, M. Karlsson, and V. Torres-Company, "Spectral interferometry with frequency combs," Micromachines **13**, 614 (2022).

[11] Y. Sun, J. Wu, M. Tan, X. Xu, Y. Li, R. Morandotti, A. Mitchell, and D. J. Moss, "Applications of optical microcombs," Adv. Opt. Photonics **15**, 86 (2023).

[12] K.-P. Ho and J. M. Kahn, "Optical frequency comb generator using phase modulation in amplified circulating loop," IEEE Photonics Technol. Lett. **5**, 721–725 (1993).

[13] A. Shams-Ansari, G. Huang, L. He, Z. Li, J. Holzgrafe, M. Jankowski, M. Churaev, P. Kharel, R. Cheng, D. Zhu, N. Sinclair, B. Desiatov, M. Zhang, T. J. Kippenberg, and M. Lončar, "Reduced material loss in thin-film lithium niobate waveguides," APL Photonics **7**, 081301 (2022).

[14]C. Wei, J. Li, Q. Jia, D. Li, and J. Liu, "Ultrahigh-Q lithium niobate microring resonator with multimode waveguide," Opt. Lett. **48**, 2465 (2023).
[15]Y. Hu, M. Yu, B. Buscaino, N. Sinclair, D. Zhu, R. Cheng, A. Shams-Ansari, L. Shao, M. Zhang, J. M. K. M. Lončar, and M. Lončar, "High-efficiency and broadband on-chip electro-optic frequency comb generators," Nat. Photonics **16**, 679–685 (2022).
[16]J. Zhang, C. Wang, C. Denney *et al.*, "Ultrabroadband integrated electro-optic frequency comb in lithium tantalate," Nature **637**, 1096–1103 (2025).
[17]G. Ghione, *Semiconductor Devices for High-Speed Optoelectronics* (Cambridge University Press, Cambridge, 2009).
[18]The microwaves travel with the phase velocity, as they have a single frequency component. However, the optical propagation is governed by the group velocity, as the modulation broadens the pump light and a wave packet forms. The same applies to traveling phase modulators regarding the velocity matching condition.[19]
[19]R. Spickermann, S. Sakamoto, and N. Dagli, "In traveling wave modulators which velocity to match?" in *Conference Proceedings LEOS'96 9th Annual Meeting IEEE Lasers and Electro-Optics Society* (IEEE, 1996), Vol. 2, pp. 97–98.
[20]The normalized phase shift $|\phi_r|/\phi_{\text{norm}}$ can be calculated with Eqs. (2)–(6). Their dependency on the unitless quantities stated in the text is explicitly visible, except for the expressions $\omega_m t_j$ and $V^{\pm}/V_0$. The dependency of the latter expression can be followed with the formulas in Appendix B. The former expression contains the entrance times t_j, which are linear combinations of the optical transit times for one round trip, t_r, and a modulation segment, $t_e = L_e/v_o$. As the expressions $\omega_m t_r = 2\pi k$ and $\omega_m t_e = 2\pi L_e/L_r^{\min}$, the phasor $\omega_m t_j$ only depends on the unitless quantities listed in the text.
[21]F. Kaufmann, G. Finco, A. Maeder, and R. Grange, "Redeposition-free inductively-coupled plasma etching of lithium niobate for integrated photonics," Nanophotonics **12**, 1601–1611 (2023).
[22]A. Volpini *et al.*, "Electrode optimization for on chip resonant electro-optic frequency combs," in CLEO/Europe-EQEC (IEEE, 2025).
[23]The microwave source in the experiment, consisting of a synthesizer and circulator, is equivalent to the voltage source with internal impedance as used in the theoretical model.[24]
[24]K. Kurokawa, "Power waves and the scattering matrix," IEEE Trans. Microwave Theory Tech. **13**, 194–202 (1965).
[25]We assumed an optical ring with a free spectral range (FSR) of 20 GHz, a group index n_o of 2.0, and circular bendings with a radius of 60 μm. The electrodes can maximally cover the straight sections of the ring. The modulation frequency f_m is 20 GHz. The transmission lines have a characteristic impedance Z_0 of 100 Ω, microwave losses α_m of 173 Np m^{-1} (15 dB cm^{-1}), and effective index n_m of 2.3.
[26]D. M. Pozar, *Microwave Engineering*, 4th ed. (Wiley, Hoboken, NJ, 2012).
[27]M. Steer, *Microwave and RF Design: Transmission Lines*, 3rd ed. (NC State University, 2019), Vol. 2.
[28]We use the complex notation to simplify the derivation and formulas. The physical quantities are given by the real part of the complex fields.
[29]E. Olson, "On computing the average orientation of vectors and lines," in *2011 IEEE International Conference on Robotics and Automation* (IEEE, 2011), pp. 3869–3874.
[30]D. A. Frickey, "Conversions between S, Z, Y, H, ABCD, and T parameters which are valid for complex source and load impedances," IEEE Trans. Microwave Theory Tech. **42**, 205–211 (1994).
[31]M. Steer, *Microwave and RF Design: Networks*, 3rd ed. (NC State University, 2019), Vol. 3.
[32]N. D. Orloff, N. Popovic, J. A. Drisko, A. Stelson, C. A. E. Little, J. C. Booth, J. Mateu, and C. J. Long, "How to extract distributed circuit parameters from the scattering parameters of a transmission line," in *2017 90th ARFTG Microwave Measurement Symposium (ARFTG)* (IEEE, 2017), pp. 1–5.